

# In-depth Inhomogeneities in CIGS Solar Cells: Identifying Regions for Performance Limitations by PIXE and EBS

*Victoria Corregidor<sup>1,2\*</sup>, M. Alexandra Barreiros<sup>3</sup>, Pedro M.P. Salomé<sup>4,5</sup>, Luís C. Alves<sup>1</sup>*

1 C2TN, Campus Tecnológico e Nuclear, Instituto Superior Técnico, Universidade de Lisboa, E.N. 10, 2686-953 Sacavém, Portugal

2 IPFN, Instituto Superior Técnico, Universidade de Lisboa, E.N. 10, 2686-953 Sacavém, Portugal

3 Laboratório Nacional de Energia e Geologia, UME, Estrada do Paço do Lumiar, 22, 1649-038 Lisboa, Portugal

4 International Iberian Nanotechnology Laboratory, 4715-330 Braga, Portugal

5 Departamento de Física, Universidade de Aveiro, Aveiro 3810-193, Portugal

\*corresponding author:

Victoria Corregidor

C2TN, Centro de Ciências e Tecnologias Nucleares

<https://doi.org/10.1021/acs.jpcc.1c02731>  
© 2021 American Chemical Society

Campus Tecnológico e Nuclear, Instituto Superior Técnico, University of Lisbon

Estrada Nacional 10 (km 139,7), 2695-066 Bobadela, Portugal

e-mail: [vicky.corregidor@ctn.tecnico.ulisboa.pt](mailto:vicky.corregidor@ctn.tecnico.ulisboa.pt)

Tel. +351 21 994 6080

Fax: + 351 21 994 6285

ORCID: /0000-0001-8323-0634

KEYWORDS: CIGS, thin solar cell, defects, composition, IBA techniques, depth profiling

ABSTRACT. When considering materials to be used as active layers in solar cells, an important required parameter is the proper knowledge of their elemental composition. It should be heavily controlled during growth in order to obtain the desired bandgap and to decrease recombination defects and then increase the solar cell electrical performance. Ion beam analytical techniques and, in particular particle-induced X-ray emission (PIXE) and elastic backscattering spectrometry (EBS), are quite suitable to determine the thickness and composition of such active layers. Furthermore, if these techniques are performed using a nuclear microprobe, lateral and in-depth inhomogeneities can be clearly observed from 2D maps. In many cases, composition variations can be detected from the classical 2D maps obtained from the PIXE spectra. In this work, it is shown how the in-depth variations can also be studied when considering 2D maps reconstructed from the EBS spectra. Such variations are derived from processing conditions and can be related to: i) composition, ii) thickness, iii) roughness, iv) other non-trivial issues. Examples obtained on Cu(In,Ga)Se<sub>2</sub> based cells are presented and discussed. Furthermore, the combination of ion beam analytical techniques such as PIXE and EBS is shown to be a competitive and alternative method to those more used and established techniques such as X-ray fluorescence for checking the average composition of the solar cells active layers or SIMS for the determination of elemental depth profile.

## ***1. Introduction***

Ion beam analytical (IBA) techniques, in particular PIXE (particle-induced X-ray emission) and EBS (elastic backscattering spectrometry), are commonly used for determining elemental composition on a wide range of materials and devices <sup>1</sup>. PIXE enables to quantify a sample elemental concentration from the peaks intensities of the characteristic X-ray emitted from the atoms during particle irradiation. PIXE is a very sensitive technique capable of providing information for elements of atomic number down to  $Z=11$  <sup>2-3</sup>, and contrary to many other techniques, it does not require any calibration sample. EBS is quite sensitive to depth elemental profiling, allowing for sample in-depth composition determination by recording the backscattered ions' energy <sup>1</sup>. PIXE major drawbacks are that it does not provide depth resolved information and there might be an overlap of the X-ray characteristic energy values. EBS major drawbacks are the low sensitivity for light elements in a high  $Z$  matrix and, in some cases, the difficulty to distinguish elements with similar atomic number at different depths. Such disadvantages can be overcome by combining all obtained data during particle irradiation and performing a simultaneous analysis, using the Total IBA concept <sup>4</sup>. The data to be combined can be acquired using different experimental conditions (beam energy or beam particles), or other ion beam nuclear based methods such as nuclear reaction analysis (NRA) or elastic recoil detection analysis (ERDA).

The IBA techniques capabilities are enhanced when coupled to a scanning nuclear microprobe <sup>5</sup>, due to: i) the possibility to focus the beam to sub-micrometer spot sizes <sup>6</sup> (sometimes deep sub-micron <sup>7</sup>), ii) the possibility of rastering a specimen area under analysis to determine elemental distributions in one or two dimensions in a fully

quantitative manner while adding imaging capabilities. Furthermore, the nuclear microprobes are usually equipped with both X-ray and particle detectors allowing for simultaneous acquisition of PIXE and EBS spectra, making it possible to perform the combined analysis of the collected data. See for example refs. 8-9 where perovskite thin films were characterized using this procedure in order to get depth compositional profile.

Nuclear microprobes also allow determining the interactions of macrostructured bioactive glasses with biological medium <sup>10</sup> or for 3D imaging and quantification of metal nanoparticles in light matrix specimens, such as biological cells. Chen et al. <sup>11</sup> obtained 3D high-resolution imaging on the distribution of gold nanoparticles inside a cell by using 1.6 MeV helium ions and combining scanning transmission ion microscopy, forward scattering transmission ion microscopy and elastically backscattered ions. Also, Vasco et al. <sup>12</sup> developed a software tool, MORIA, to display metal nanoparticles in cells in a 3D environment using the depth distribution obtained from EBS spectra.

Similar results are not yet available for medium and high Z matrices, however such milestone could be reached by performing a 3D visualization of the elemental in-depth information obtained after combining data from the PIXE and EBS spectra for each map pixel. The combination of, at least, these two IBA techniques will be essential for having 3D information on medium and high Z matrices, as these technique provide the required complementary information.

This work shows how non-homogeneous regions, unnoticed or barely distinguishable in the elemental distribution maps obtained by PIXE, can be exposed through the 2D EBS maps obtained at a certain fixed sample depth scale.

Such possibility is extremely useful in some structures and devices where homogeneity is needed at the surface and in depth for a proper operation. Such an example is the complex semiconductor multilayer structures used in Cu(In,Ga)Se<sub>2</sub> (CIGS) based solar cells, where both lateral and depth variation of composition originate several problems such as band gap fluctuations, leading to significant open circuit voltage losses<sup>13-14</sup>. Several authors have determined the in-depth elemental gradient, due to Ga and In variations<sup>15-18</sup> or Cu content<sup>19</sup>, however depending on the manufacturing technique used, artifacts and inconsistencies can still be evaluated when using micrometer resolved analytical methods. Previous research studies, using a broad ion beam, have demonstrated the suitability of IBA techniques to characterize these type of cells<sup>8-9, 15-16, 20-21</sup>, obtaining similar Ga and In depth profiles to those obtained by other techniques such as secondary ion mass spectroscopy (SIMS)<sup>22-23</sup>, with the advantage of being non-destructive and that do not require any special sample preparation.

According to “Best Research-Cell Efficiency Chart” from NREL<sup>24</sup>, the record efficiency for research cells based on CIGS is 23.4%. CIGS-based solar cells can be easily found in the market, being a competitor of other thin film technologies based on CdTe or a-Si. Furthermore, CIGS cells are good candidates for the development of tandem solar cells with another emerging technology: perovskite solar cells<sup>25</sup>. Many of the research efforts in this technology are made to control and to know the composition of the absorber and buffer layers, but the knowledge of in-depth elemental distribution in finished cells needs further investigation.

Looking for micro-inhomogeneities and composition defects, different CIGS solar cells devices were analyzed by means of IBA techniques in a nuclear microprobe and the obtained results are presented in this work. In-depth compositional variations were

found out, some of them related to the manufacturing processes, that can act as active electric and optoelectronic defects, being the main culprits for solar cell efficiency limitations. Therefore, expanding the family of techniques that can probe such properties is always looked for by the research community.

## **2. Materials and Methods**

EBS and PIXE measurements were performed at normal incidence using an Oxford Microbeams nuclear microprobe<sup>26</sup>. X-rays were detected with a 30 mm<sup>2</sup> Bruker SDD detector with 145 eV resolution, positioned at 135° with the beam direction and at a distance of 20 mm from the sample while the backscattered particles were detected with a 200 mm<sup>2</sup> PIPS detector with 30 keV resolution, positioned at 140° scattering angle in Cornell geometry and at a distance of 50 mm from the sample. Proton beams were generated from a 2.5 MV single-ended Van de Graaff accelerator.

Solar device structures based on CIGS were prepared as described in 22, with the CIGS layer grown using a standard co-evaporation process. The EBS and PIXE measurements were performed in finished solar cells, that is, the structure comprises a soda-lime glass substrate (SLG) of 1 mm thick with a Mo back contact (350 nm), followed by the CIGS absorbing layer (1700 nm), CdS and i-ZnO buffer layers (70 and 90 nm, respectively), the ZnO:Al front contact (350 nm) and contacting metal grids Ni/Al/Ni (100 nm /3000 nm/ 100 nm) each of them occupying 2.5 % of the total area. The thickness values presented are nominal values not reflecting final thickness values as they vary from solar cell to solar cell depending on the processing conditions and fluctuations in the growth process, as described in 22.

For their characterization and with the aim of optimizing the depth-resolved information, 900 keV or 1 MeV (nominal energy) proton beams with about 100 pA

beam current were used. With these energy values and considering the thickness mentioned above, the EBS spectra can give information up from the top electrode (ZnO:Al) down to the SLG substrate, being capable of probing the full device. Typical ion beam spatial resolution is  $3 \times 4 \mu\text{m}^2$ .

The OMDAQ software package <sup>27</sup> was used for beam control, data acquisition and post-data treatment. 2D-PIXE and EBS maps were obtained using the listmode playback mode by selecting the desired regions of interest (ROIs) in each spectrum.

Maps and point PIXE spectra were analyzed using the GUPIX <sup>28</sup> software to extract the elemental peak areas that are used as input data in the NDF v9.6a code <sup>29</sup>, which simultaneously fits the PIXE and the EBS spectra providing for a self-consistent solution. Thickness values are given in areal density (that is,  $\text{at}/\text{cm}^2$ ), the standard units in IBA analyses. For guidance, an estimation of the thickness values is presented in nm units considering, for compounds densities, the weighted average of the bulk densities. The default uncertainty considered in NDF for PIXE is 10%. NDF fit is done minimizing a  $\chi^2$  function, a complete analysis of RBS (Rutherford backscattering spectrometry) accuracy can be found in <sup>30</sup>.

High-resolution cross section images were obtained by scanning electron microscopy (SEM) using a FEI Nova Nano 650 system using acceleration voltages of 3 kV and 5 kV. The cross sections were achieved by mechanically cleaving the solar cells <sup>31</sup>. This process creates non uniform cuts and to counter this, large areas are analysed, hence, the image presented here is representative of the analysed area.

### **3. Results**

The 2D-PIXE elemental distribution maps for a CIGS device are shown in figure 1. There are two regions (A and B), or clusters, with a dimension of 20-30  $\mu\text{m}$  with

elemental concentration that varies significantly from the rest of the area under study. These maps were recorded using a 900 keV proton beam over a region of  $530 \times 530 \mu\text{m}^2$ . We note that different areas were analyzed and similar abnormal regions were found throughout the whole sample. In figure 2a, it is shown the average EBS spectrum recorded during the experiment when scanning the entire  $530 \times 530 \mu\text{m}^2$  area. The fit of this EBS spectrum, considering as input data the PIXE concentrations of each element obtained from the average PIXE spectrum, shows a layer of  $3924 \times 10^{15} \text{ at/cm}^2$  ( $\sim 737$  nm) of ZnO (oxygen rich) followed by a  $330 \times 10^{15} \text{ at/cm}^2$  ( $\sim 73$  nm) of CdS, a CIGS film of about  $8474 \times 10^{15} \text{ at/cm}^2$  ( $\sim 1680$  nm) and a  $1501 \times 10^{15} \text{ at/cm}^2$  ( $\sim 234$  nm) single layer of molybdenum which shows a spreading towards the SLG of  $1097 \times 10^{15} \text{ at/cm}^2$  (211 nm). Notice that although EBS and PIXE have no sensitivity to chemical bonds the fitting model of NDF allows defining molecules (instead of elements) with fixed or variable stoichiometry, the depth range where elements/molecules can exist and the concentration range in which they can vary. This procedure provides a sounder problem solution while saving computer processing time<sup>32</sup>. In figure 2a “ZnO, CdS, CIGS and SLG” are labelled as compounds: these are treated as “logical elements” by the computation engine of NDF, which thus imposes “chemical priors” onto the data (as discussed by Butler<sup>33</sup>). Individual spectra for Zn, O, Cd, S are shown in the figure, nevertheless Cu, Ga, In and Se signals has been replaced by their sum and labelled as “CIGS” for a better visualization of the different layers. Same procedure was done for SLG compound.

The obtained depth profile, jointly with the concentration values, are shown in figure 2b. Regarding the CdS layer, the obtained data (90% CdS and 10% ZnO+CIGS) can be explained considering the layer thickness and roughness of the layers observed in figure 2c. As such, the resulting fit assigns to this layer small amount of the compounds found

in the neighboring layers. Furthermore, the obtained average CIGS composition is  $\text{Cu}_{0.79}(\text{In}_{0.73}\text{Ga}_{0.27})\text{Se}_{1.72}$  ( $[\text{Cu}]/([\text{Ga}]+[\text{In}])$  ratio is 0.79 and  $[\text{Ga}]/([\text{Ga}]+[\text{In}])=0.27$ ), aligned with expected values extracted from XRF after growth process. The estimated thickness and composition values are within margin uncertainties of the expected nominal values.

2D-PIXE maps (Figure 1) show small regions with high concentration of silicon and molybdenum and a reduced, or inexistent, signal from the other elements belonging to the active, CdS and ZnO, layers. Regarding region A, visible in almost all the 2D-PIXE maps, a point analysis was performed (see figure 3). This region consists of about  $1818 \times 10^{15} \text{ at/cm}^2$  ( $\sim 283 \text{ nm}$ ) of Mo on top of the SLG substrate (see figure 3a), where it is also possible to detect a small amount of Argon atoms (1.5 at.%), as can be seen in the PIXE spectrum (figure 3b), jointly with the other elements from the glass (Ca, K and Si). Region B in figure 1 can also be observed in all 2D maps, with different dimensions, being larger in the Si map, probably due to the beam straggling effect (as the proton beam penetrates sample, the slowing down is accompanied by a spread both, in space and energy). This region composition will be discussed in detail later.

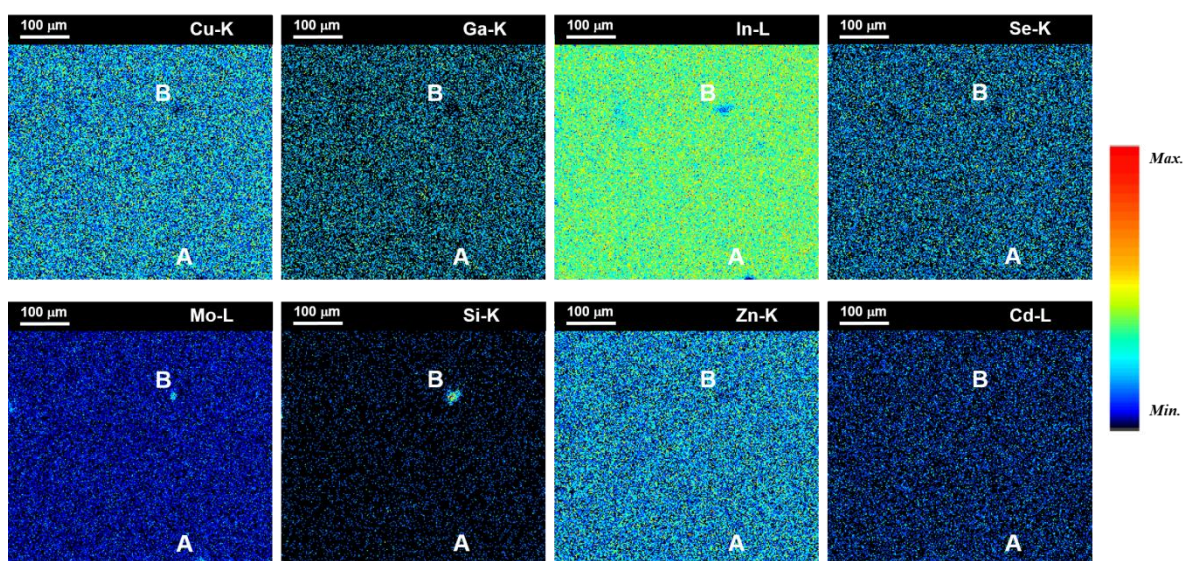


**Figure 1.** 2D elemental distribution maps ( $530 \times 530 \mu\text{m}^2$ ) from PIXE spectra (900 keV proton beam), for the elements present in the CIGS absorber layer (Cu, In, Ga and Se), ZnO, Mo layers and SLG (Si). Labels A and B are inhomogeneous regions referred in the text.

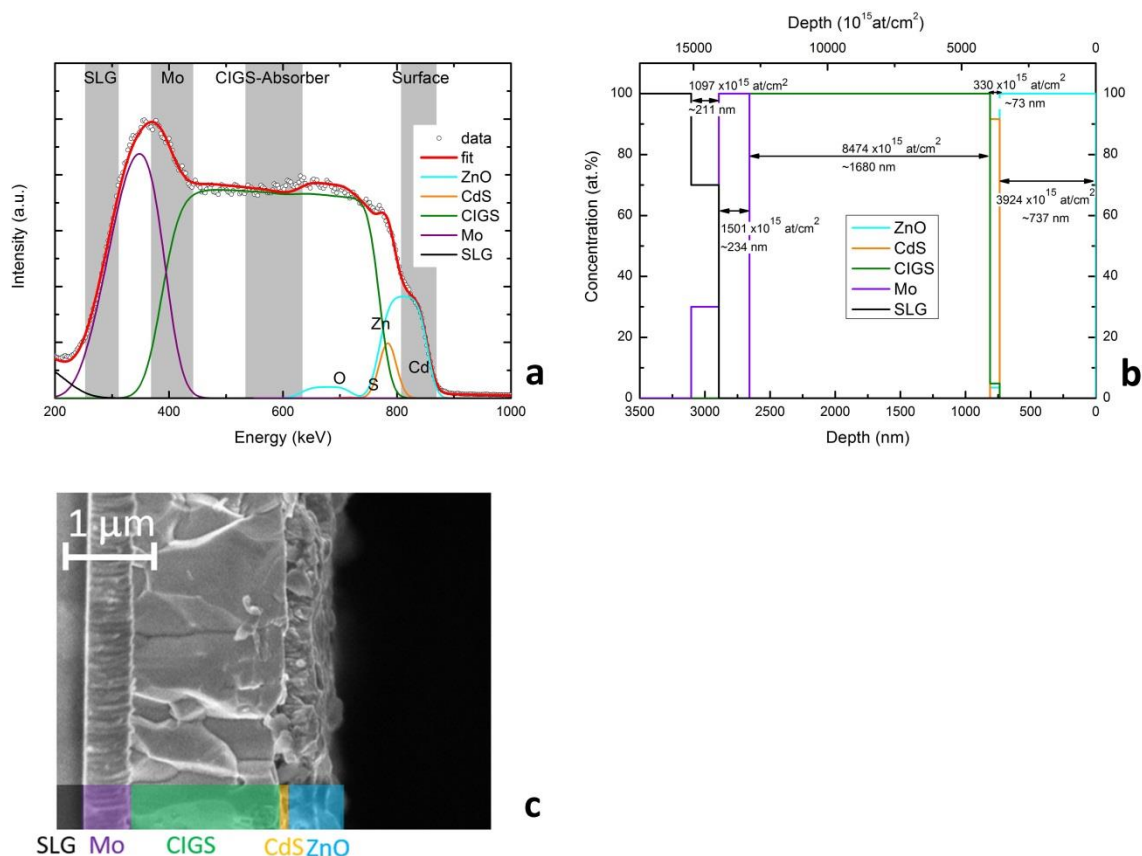


**Figure 2.** a. EBS spectrum, fit and partial spectra of the layers and SLG contribution. For reasons of clarity, the CIGS partial spectrum is the sum of the individual Cu, Ga, In and Ga signals contributions. The spectrum is the one recorded at 900 keV over an area of  $530 \times 530 \mu\text{m}^2$ , shown in figure 1. Shaded areas refer the ROIs used to obtain the maps shown in figure 4; b. Depth profiles for the different layers obtained from the fit; c. Cross-section SEM image of the CIGS solar cell.

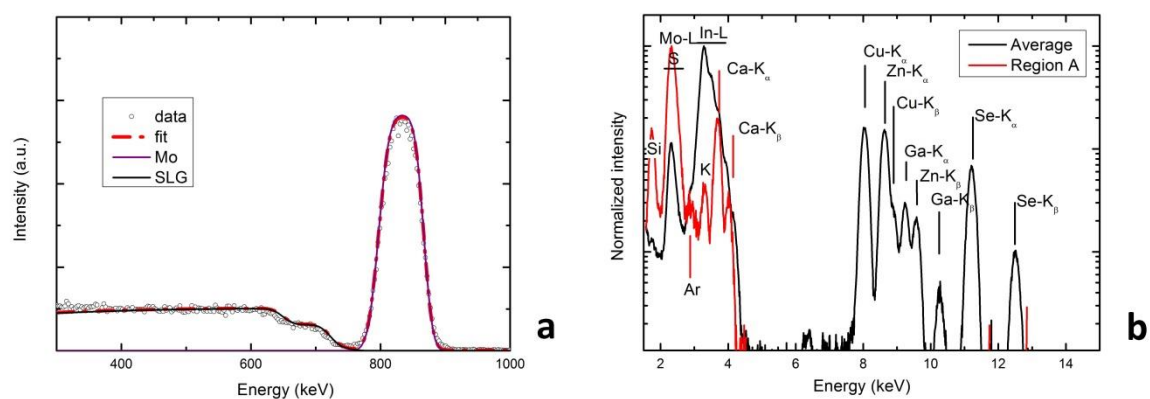


**Figure 3.** a. EBS spectrum and fit of region A (see figure 1); b. PIXE spectrum from region A, for a better comparison PIXE spectrum for the average scan has been included.

2D maps can also be obtained from the ROIs selected in the average EBS spectrum (shown in figure 2a in grey colour). The maps obtained from these ROIs are shown in figure 4, which have been labeled (according to the average EBS spectrum) as surface, CIGS-absorber layer, Mo contact and SLG. Nevertheless, although EBS provides information about the elemental depth profile, the inhomogeneities detected in the maps cannot be straightforward related to these layers.

In these 2D-EBS maps inhomogeneous regions can be found, some of them are visible in all maps and others only in some of them. Furthermore, previous mentioned regions (A and B) are clearly observed in the 2D-EBS maps but new regions (C and D) are not visible, or barely distinguishable, in any of the PIXE maps (figure 1). These heterogeneities were found to be related to both, layer thickness and composition irregularities.

A close view of regions B and C is shown in figure 5a, and a detailed observation of the elemental distribution in these regions was made. Five point analyses (within the

system resolution) were performed, labelled as 1, 2, 3, 4 and 5; EBS and PIXE spectra obtained on these points are shown in Figure 5 (b-e), where, for a better comparison, the average EBS fitted spectrum (Figure 2a) has been included.

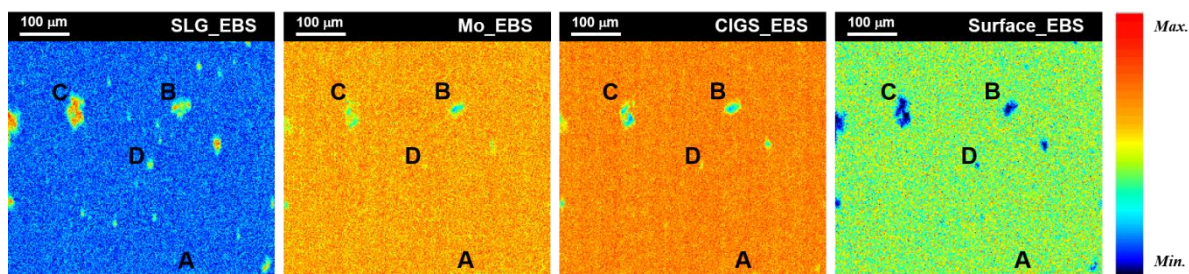


**Figure 4.** 2D maps ( $530 \times 530 \mu\text{m}^2$ ) from EBS spectra (900 keV proton beam), considering the ROIs shown in the EBS spectrum (figure 2a). Labels A, B, C and D are inhomogeneous regions referred in the text.

Region B can be related to a SLG substrate irregularity (point 2), considering the results from the EBS and PIXE spectra. PIXE spectrum shows as main peaks those associated with Si and Ca (from SLG) and also peaks from the other elements of the cell are observed. Furthermore, the corresponding EBS signal starts at about 820 keV, which is compatible with the presence of glass at the surface. Around this point 2, it seems that the CIGS film grew normally, with a uniform thickness, similar to that obtained for the entire map.

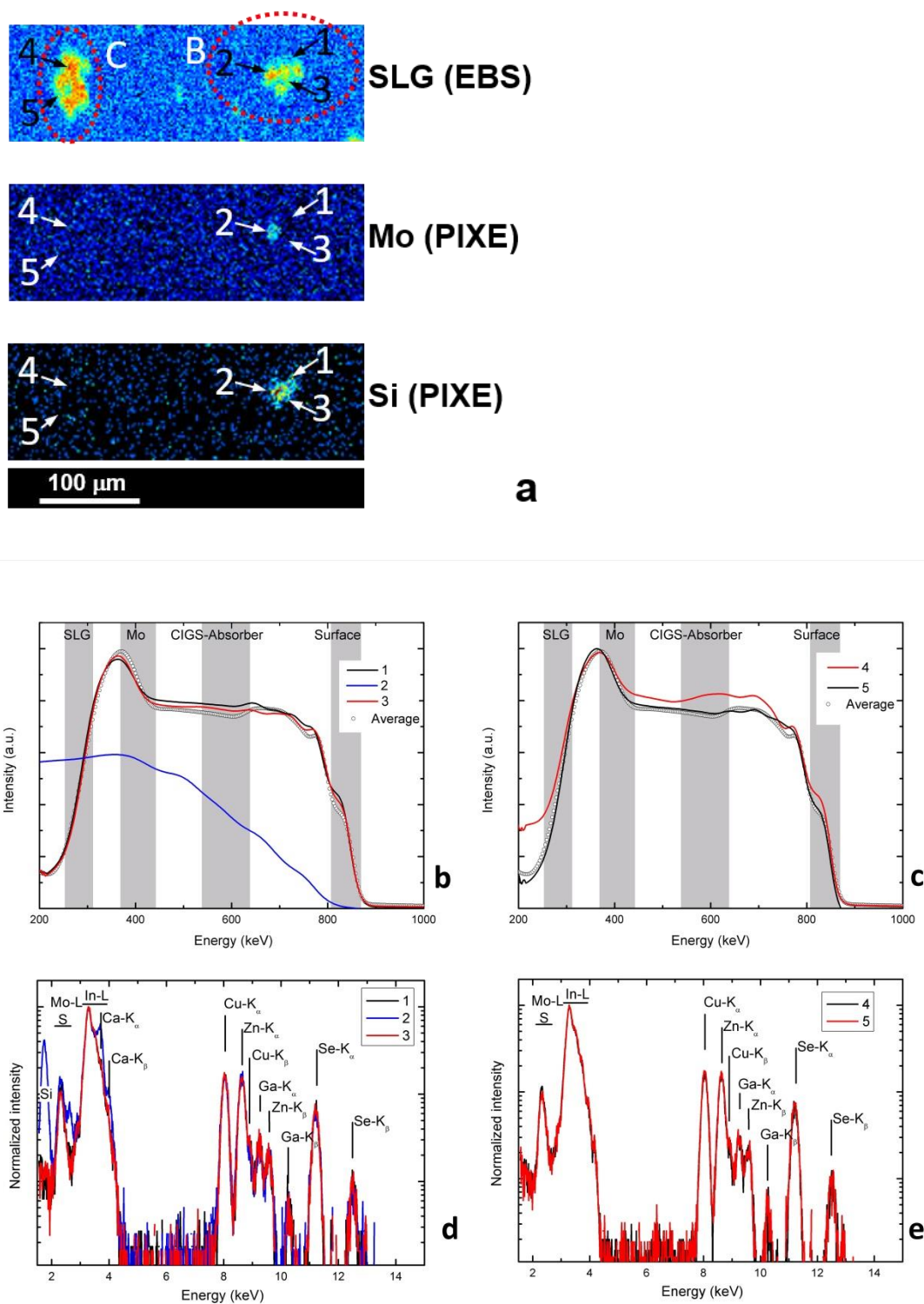


**Figure 5.** a. Close view of the 2D maps showing regions B and C (SLG, Mo and Si) from figures 1 and 4. Sites of point analyses performed are identified by numbers 1-5. b-e. EBS (b and c) and PIXE spectra (d and e) for each point.

Considering the EBS signals, the inhomogeneities of region B (points 1 and 3) are related to thickness variations of the top layers containing Zn and Cd. According to the EBS fit, the CdS and ZnO layers (surface layers) are thicker for point 3 than for point 1 ( $4691 \times 10^{15}$  at/cm<sup>2</sup> (~890 nm) and  $4365 \times 10^{15}$  at/cm<sup>2</sup> (~825 nm) respectively), being both slightly larger than the average value ( $4254 \times 10^{15}$  at/cm<sup>2</sup> (~810 nm)). Regarding the CIGS layer, although the thickness value is almost the same, the concentration of Se and In is slightly higher than that obtained for the average region, increasing thus the individual contributions to the EBS spectra.

In region C no signal from the SLG substrate was detected by PIXE. Points 4 and 5 have similar thickness values for CdS and ZnO layers, being also similar to that obtained for the average region. Nevertheless, point 4 exhibits higher Zn concentration (about 60 at.%) than point 5, (50 at.% of Zn). Concerning the active CIGS layer, in both points the thickness and composition values are quite close to that obtained for the average map. However, the Mo signal is wider, particularly for point 4, then contributing to the higher intensity signal and contrast observed in figure 5a for the SLG ROI. This indicates glass surface microscale irregularities and the corresponding variation of the deposited Mo layer.

Analogous information can be extracted from the analysis of other CIGS solar cell. Figure 6 shows the elemental distribution maps ( $750 \times 750 \mu\text{m}^2$ ) obtained from PIXE spectra of the absorber layer constituents (Cu, In, Ga and Se) from another CIGS device. The maps indicate a homogeneous distribution for all the elements present in the cell within the system resolution. Figure 7a shows the corresponding average EBS spectrum recorded during the experiment and the fit, considering as input data the concentrations of each element obtained by GUPIX. As shown in figure 7b, the best fit

consists of a  $3340 \times 10^{15}$  at/cm<sup>2</sup> (~611 nm) film of ZnO, followed by a  $350 \times 10^{15}$  at/cm<sup>2</sup> (~78 nm) layer of ZnO and CdS (with composition of 20 at.% and 80 at.% respectively), then a CIGS film of about  $7920 \times 10^{15}$  at/cm<sup>2</sup> (~1587 nm) and a single Mo layer of  $976 \times 10^{15}$  at/cm<sup>2</sup> (~152 nm) thick. This layer shows also a  $1700 \times 10^{15}$  at/cm<sup>2</sup> (~324 nm) mixed layer, related to substrate roughness. Furthermore, the composition obtained for this layer is  $\text{Cu}_{0.93}(\text{In}_{0.71}\text{Ga}_{0.29})\text{Se}_{1.92}$  ( $[\text{Cu}]/([\text{Ga}]+[\text{In}])=0.93$  and  $[\text{Ga}]/([\text{Ga}]+[\text{In}])=0.29$ ). Equivalent results for both, composition and thicknesses, were obtained in points randomly selected in the 2D-PIXE maps.

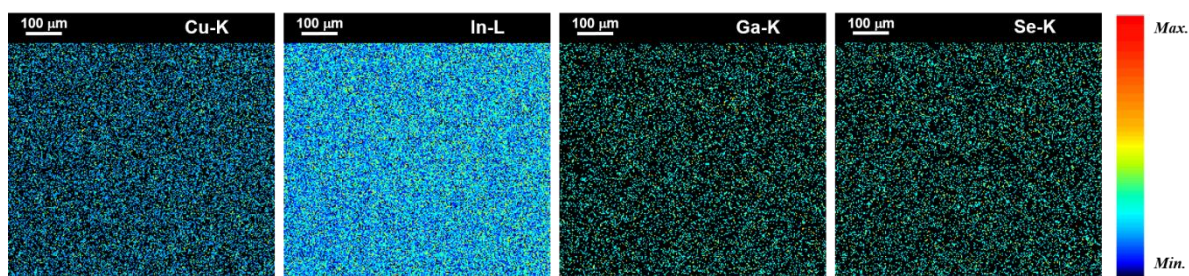


**Figure 6.** 2D elemental distribution maps ( $750 \times 750 \mu\text{m}^2$ ) from PIXE spectra (1 MeV proton beam), for the elements present in the CIGS absorber layer: Cu, In, Ga and Se.

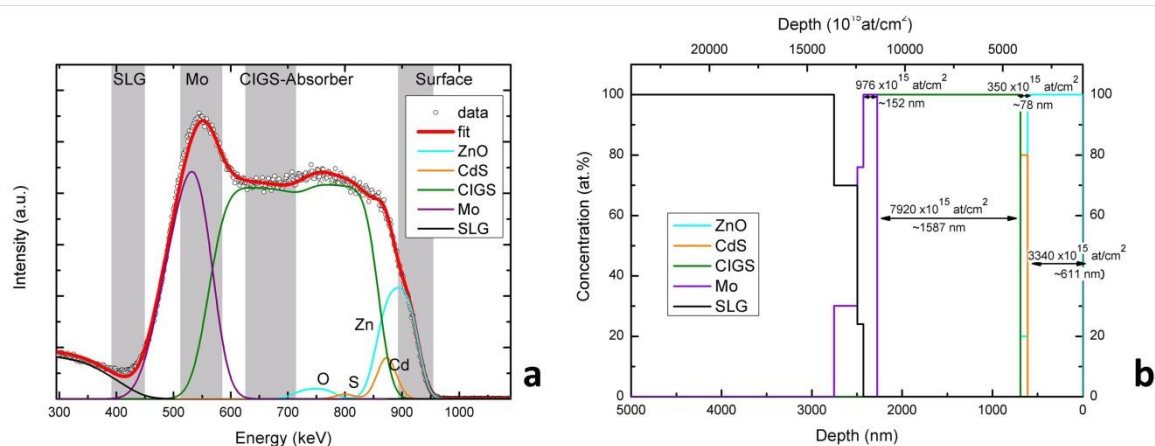


**Figure 7.** a. EBS spectrum, fit and partial spectra of the layers and SLG contribution. For reasons of clarity, the CIGS partial spectrum is the sum of the individual Cu, Ga, In and Ga signals contributions. The spectrum is the one recorded at 1 MeV over an area of  $750 \times 750 \mu\text{m}^2$ , shown in figure 6. Shaded areas refer the ROIs used to obtain the maps shown in figure 8; b. Depth profiles for the different layers obtained from the fit.

Figure 8 shows the 2D-EBS maps obtained from the ROIs defined in figure 7a, as previously discussed. In these EBS maps inhomogeneous regions can be found, some of which are visible in all maps (labelled as I), others in some maps (II), and others in only one of them (III), and barely distinguishable in any of the PIXE maps (figure 6). These heterogeneities are related to both, thickness and composition irregularities as it can be observed in figure 9, where PIXE and EBS spectra recorded on points I, II (underlined in figure 8) and III are shown.

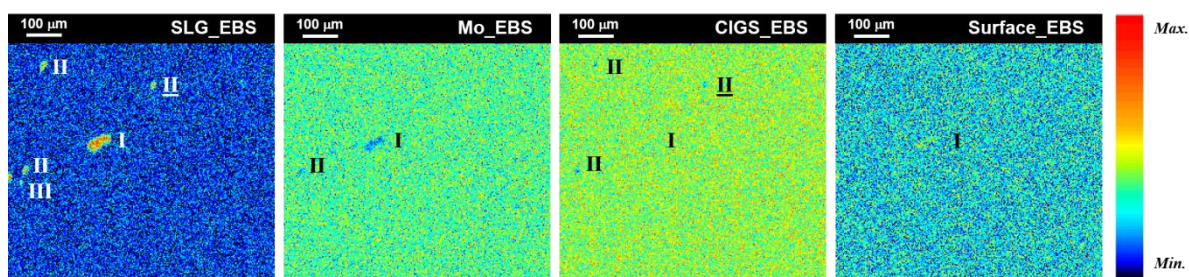


**Figure 8.** 2D maps ( $750 \times 750 \mu\text{m}^2$ ) from EBS spectra (1 MeV proton beam), considering the ROIs shown in the EBS spectrum (figure 7). Labels I, II and III are inhomogeneous regions referred in the text.

Considering the PIXE spectra, the main differences are found in the low energy region, where peaks related to Si and Ca (from the soda lime glass substrate) are much higher for points II and III than for point I. Also, in those two points the signal at 2.3 keV is higher than for point I, which could be related to variations in the thickness of

the CdS or Mo layers, most likely to the Mo layer once variation in Cd signal is not noticed. On the other hand, point I shows a peak with low intensity at 2.3 keV while the intensities of peaks related to Se, Ga and Cu are slightly higher than in the other points.

For each analyzed point, diverse compositional profiles can be obtained, all of them quite different from the average EBS spectrum (figure 7), and from the previous analyzed CIGS cell. A small shift towards high energy is detected for point I, which could be associated with the presence at the surface of elements with atomic number higher than Zn ( $K=0.94700$ ) but, as shown in figure 7, lower than Cd ( $K=0.96883$ ) or In ( $K=0.96947$ ) as for the case of Mo ( $K=0.96358$ ), being  $K$  the kinematic factor, the energies ratio of the projectile particle and of the scattered particle<sup>34</sup>. However, the Mo signal in the PIXE spectra for point I is very weak and so, its presence at the surface can be excluded. Then, the shift can be explained considering a thin layer of ZnO (about 92 nm instead of the ~600 nm average value), resulting in the shift of the Cd signal towards higher energies. This means that due to a surface defect in that area, probably produced during the growth process, the needed thickness of ZnO layer was not achieved. The evolution of the signal in depth (drop and rise between channels 300 and 500) was not possible to determine and more data are needed to explain this behaviour.

In figure 10 it is shown the proposed fits of EBS spectra for points II and III. Both are characterized by a clear signal from the upper layers, followed by the CIGS film. In both points, an extra contribution of oxygen content had to be assumed in order to obtain a proper fit.. Point II shows a Mo profile further extending into the SLG substrate than the one observed for the average spectrum map while for point III the Mo layer seems to be thicker.

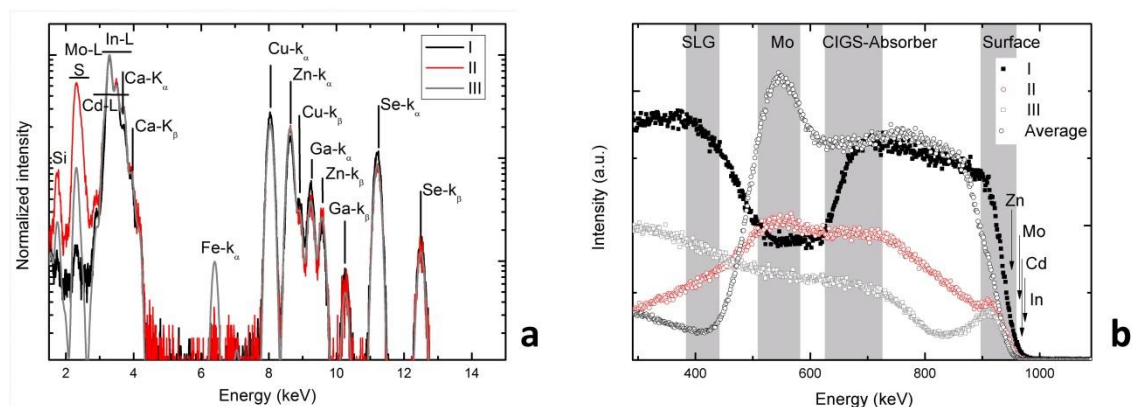


**Figure 9.** Point PIXE (a) and EBS (b) spectra (1 MeV proton beam) recorded in points I, II (underlined) and III (see figure 8). In the EBS spectrum, the surface barrier position for Zn, Mo, Cd and In are labeled.

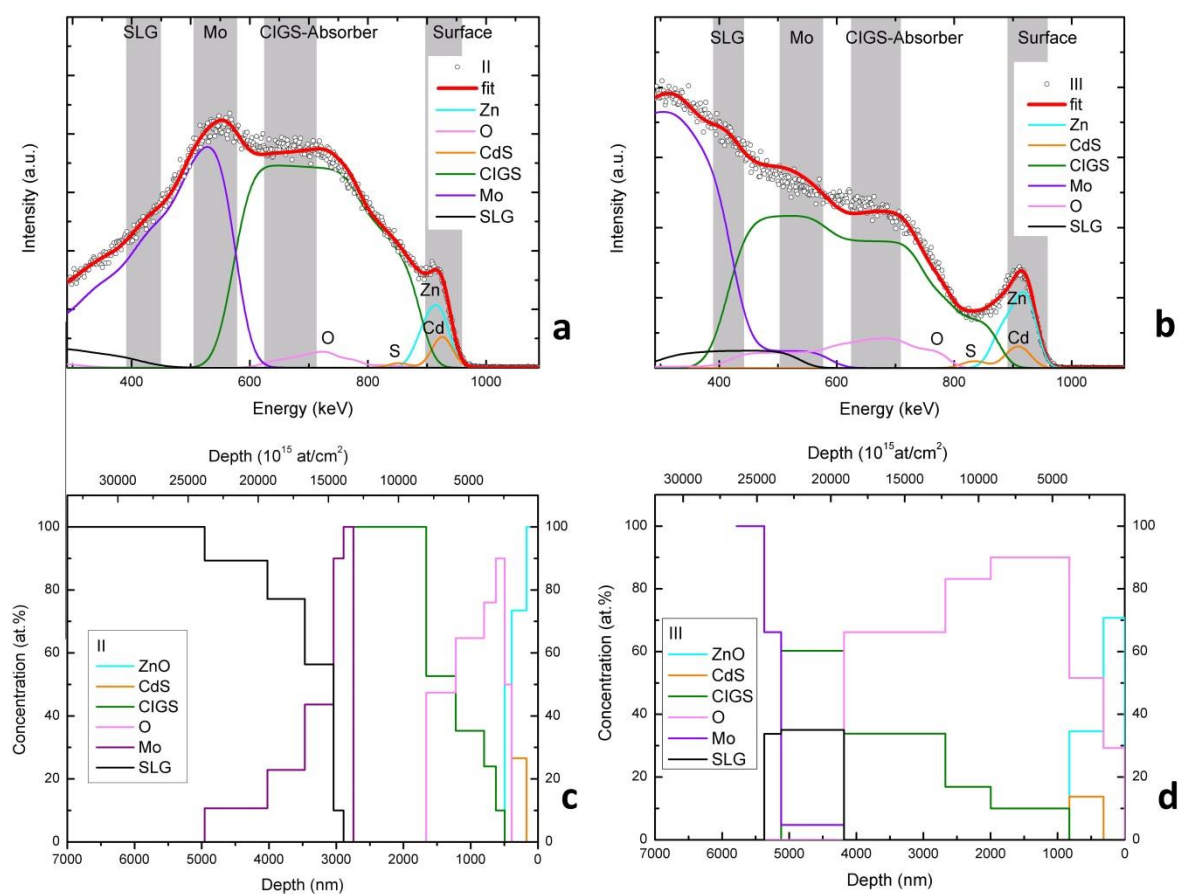


**Figure 10.** EBS spectra, fit and partial spectra of each layer: a. Point II; b. Point III. c. Depth profile for Point II; d. Depth profile for point III.

#### 4. Discussion

The use of a nuclear microprobe, where it is possible to focus and raster the particle beam, and the simultaneous acquisition of PIXE and EBS spectra allows one to visualize not only the elemental distribution over the surface (with  $\mu\text{m}$  spatial resolution) but also the elemental in-depth variations on CIGS solar cells (with resolution down to the nanometer range, depending on the species and energy of the ion beam used and layer composition [4]). Also, by combining multiple IBA spectra and using the NDF code it was possible to obtain the composition and depth profile in different scenarios, allowing both, quantitative and qualitative analyses.

Figure 3 shows a trivial defect where data from PIXE (showing the presence of Ar) were very important to unambiguously correlate this defect and the manufacturing process. Argon is used as the ionization gas during the sputtering processes of the Mo layer and the front contact<sup>22</sup>. Hence, it is likely that in region A (in figure 1) CIGS has peeled off and it is now acting as an electrical shunt and/or a dead region, being in both cases heavy detrimental for the solar cell performance.

Figures 4 and 5 show the importance of the qualitative results obtained, which correspond to heterogeneous regions revealed when using the 2D maps from EBS spectra. Those regions are related to small differences in layer thickness when compared with the average results. Too thick CdS and ZnO layers (see points 1 and 3 in figure 5) will increase the device series resistance leading to poor fill factor values and these non-uniformities should be avoided. The presence of glass at micrometer scale (see point 2 in figure 5) could be related to sample manipulation damage such as scribing for cell definition or to the growth conditions, which at this region, were not meet for a favorable growth of the layers.

On the other hand, EBS spectra (figures 9 and 10) recorded in defects shown in figure 8 are hard to fit. To obtain a fit consistent with the data, the presence of free oxygen was considered, although as Butler<sup>33</sup> pointed out, there may be two or more different solutions that provide equally good fits of simulated spectrum to experimental spectrum. To overcome the ambiguity, as Jeynes et al. showed in<sup>35</sup>, there are two approaches to constrain the solutions found: collect multiple spectra, and/or use restrict conditions in the structure, based on previous knowledge of the sample. Unfortunately, from PIXE the presence of oxygen cannot be confirmed although concentration of the visible elements acts as restrict condition. It is also known that prior to the deposition of the buffer layer, the samples are in open air for about 5 min. During this period,

oxidation and other reactions of the CIGS surface starts to occur due to both oxygen and water in ambient air <sup>36</sup>.

The proposed solution can be considered unsuitable, being more appropriate to consider the possible chemical bindings to obtain a more reliable composition (this possibility is easily accepted by the NDF code). Nevertheless the mechanisms and recombination kinetics that may occur in the CIGS/CdS interface are very dependent on the oxygen exposure, examples are: Cu and Cd interdiffusion or the formation of SeO<sub>2</sub>, CdCuS, Cu<sub>2</sub>Se compounds, among others <sup>36-40</sup>. Because of that, to obtain a reliable solution for these EBS spectra considering the presence of different compounds more information is needed, which can be obtained by other analytical techniques.

Generally speaking, several types of defects can be found in CIGS solar cells by means of IBA techniques. We have identified several defects that contribute to lower the overall optoelectronic performance demonstrated by the illuminated J-V figures of merit of solar cells: i) dead areas, i.e. CIGS regions that are not electrically active, hence there is no extraction of photo-generated current, contributing to smaller values of short circuit current density when compared with active areas; ii) non-uniform thicknesses of CdS and the window layers that can lead to variations in the charge extraction resistance, lowering the fill factor; and iii) variations in the composition of the CIGS layer itself that can lead to the creation of secondary phases, energy band gap variations, or recombination channels increasing the number of active defects and hence lowering the open circuit voltage.

Most of these defects might be related to the thickness of the different layers involved. This fact is connected to the manufacturing methods (chemical bath deposition for CdS buffer layer and sputtering for front contacts) or to the glass irregularities. It is known that when using chemical bath deposition, in certain cases,

nucleation points lead to agglomerates of colloids pre-formed in the solution reacting with the surface and leading to thick regions in those places. With regards to sputtering, this technique is also not fully conformal, as regions with different aspect ratios can lead to shadowing or other geometrical effects resulting in quite different thicknesses. In what accounts for the glass irregularities, they play an important role during the nucleation phase and the upper layers will inherit these imperfections during growth.

Another important issue to be highlighted is the time needed to obtain the results, including also the machine time. To acquire the maps with an acceptable counting statistics, about 1 hour is needed. If non-homogeneous regions are found within this period, then point analysis can take about 10 minutes. But, if the maps are being processed later using the listmode playback mode (as partially done in this work), longer runs are needed to ensure a good counting statistics in each pixel of the map. However the playback mode allows obtaining further and more detailed results in off-line conditions without further need of machine time.

There are many studies about elemental distribution using, for example, electron microscopy techniques, where cross sections are specifically prepared. When using electrons to probe samples, the penetration depth of those electrons is very low when compared with protons. The use of MeV ion beams allows imaging on finished cells in a non-destructive way, without the need of any preparation.

## **5. Conclusions**

The suitability of using low energy proton beams (~1 MeV) for the IBA characterization of the complex thin layer structures of CIGS solar cells is shown. By combining 2D maps obtained from PIXE and EBS spectra recorded in different regions of the studied solar cells, we demonstrated the in-depth detection of non-homogeneous

regions. Such identification could not be done when considering only the 2D elemental distribution maps reconstructed from the PIXE spectra.

Knowing the in-depth compositional variations in the CIGS structures is of the utmost importance as they are most certainly related to recombination centres, shunt-paths, dead areas, etc., which affect the overall solar cells performance. We have identified three types of defects: i) dead areas, ii) charge extraction variations in the buffer and transparent conductive oxide layers; and iii) different CIGS compositions that can lead to modification in the active recombination channels. The identification of these problems through Ion Beam Analysis is important as typically these issues are hard to pinpoint using only one technique.

The procedure presented in this work can be applied to other materials and devices using nuclear microprobe spectroscopy, and it allows studying final devices in a non-destructive way. This work also shows that recording multiple spectra is fundamental for extracting as much information as possible, allowing both quantitative and qualitative results. Furthermore, a good knowledge of the techniques and related analysis codes is fundamental for data interpretation. The variations now detected at certain depths in the EBS maps were found to be due both to layers overlap and signal shifts resulting from composition or thickness variation. For each singularity found, a detailed analysis was performed to ensure a self-consistent analysis. Finally, the obtained results allows considering that it will be possible to get general in-depth 2D map slices to perform a 3D image reconstruction, as already done for low  $Z$  matrix containing small quantities of heavy atoms. Although the procedure for the reconstruction of the 3D maps will require long measurement periods and data processing times, they can be shortened with, for example, the use of neural networks trained for each solar cell structure.

### **Author Contributions**

VC, L.C.A, M.A.B. – IBA experimental concept and optimization of the analysis parameters; experimental procedure; V.C. data fit and interpretation; original draft preparation. M.A.B., L.C.A. – definition of problems to solve; assistance in data fitting and results coherence; PMPS – fabrication of the cells under analysis; SEM data analysis; interpretation of data results versus electrical and optical properties.

The final manuscript version was written and reviewed with contributions from all authors. All authors have given approval to the final version of the manuscript.

### **ACKNOWLEDGMENT**

This work was partially supported by National Funds through FCT, Fundação para a Ciência e a Tecnologia, through project UIDB/04349/2020. V. Corregidor acknowledges the support from UID/Multi/04349/2019. P. M. P. Salomé acknowledges the funding of FCT through the project IF/00133/2015. This research is also supported by NovaCell – Development of novel Ultrathin Solar Cell Architectures for low-light, low-cost, and flexible opto-electronic devices project (028075) co-funded by FCT and the ERDF through COMPETE2020.

### **Notes**

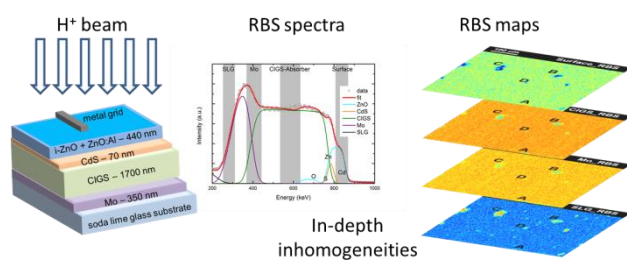
The authors declare no competing financial interest.

## References

1. Jeynes, C.; Colaux, J. L., Thin Film Depth Profiling by Ion Beam Analysis. *Analyst* **2016**, *141*, 5944-5985.
2. Grime, G. W.; Zeldin, O. B.; Snell, M. E.; Lowe, E. D.; Hunt, J. F.; Montelione, G. T.; Tong, L.; Snell, E. H.; Garman, E. F., High-Throughput Pixe as an Essential Quantitative Assay for Accurate Metalloprotein Structural Analysis: Development and Application. *Journal of the American Chemical Society* **2020**, *142*, 185-197.
3. Šmit, Ž., Physics Beyond Pixe. *Nuclear Instruments and Methods in Physics Research Section B: Beam Interactions with Materials and Atoms* **2020**, *477*, 13-18.
4. Jeynes, C.; Palitsin, V. V.; Kokkoris, M.; Hamilton, A.; Grime, G. W., On the Accuracy of Total-Iba. *Nuclear Instruments and Methods in Physics Research Section B: Beam Interactions with Materials and Atoms* **2020**, *465*, 85-100.
5. Breese, M. B.; Jamieson, D. N.; King, P. J., *Materials Analysis Using a Nuclear Microprobe*: Sussex, 1996.
6. Jallot, E.; Lao, J.; John, Ł.; Soulié, J.; Moretto, P.; Nedelec, J. M., Imaging Physicochemical Reactions Occurring at the Pore Surface in Binary Bioactive Glass Foams by Micro Ion Beam Analysis. *ACS Applied Materials & Interfaces* **2010**, *2*, 1737-1742.
7. Watt, F.; Chen, X.; Vera, A. B. D.; Udagama, C. N. B.; Ren, M.; Kan, J. A. v.; Bettiol, A. A., The Singapore High Resolution Single Cell Imaging Facility. *Nuclear Instruments and Methods in Physics Research Section B: Beam Interactions with Materials and Atoms* **2011**, *269*, 2168-2174.
8. Barreiros, M. A.; Alves, L. C.; Brites, M. J.; Corregidor, V., Depth Profile by Total Iba in Perovskite Active Layers for Solar Cells. *Nuclear Instruments and Methods in Physics Research Section B: Beam Interactions with Materials and Atoms* **2017**, *404*, 211-218.
9. Brites, M. J.; Barreiros, M. A.; Corregidor, V.; Alves, L. C.; V. Pinto, J.; Mendes, M. J.; Fortunato, E.; Martins, R.; Mascarenhas, J., Ultrafast Low-Temperature Crystallization of Solar Cell Graded Formamidinium-Cesium Mixed-Cation Lead Mixed-Halide Perovskites Using a Reproducible Microwave-Based Process. *ACS Applied Energy Materials* **2019**, *2*, 1844-1853.
10. Soulié, J.; Hardy-Dessources, A.; Nedelec, J.-M.; Jallot, E., 3d Organized Macroporous Bioactive Glasses: A Study of Pore Size Effect on Physicochemical Reactivity by Micro-Pixe-Rbs. *The Journal of Physical Chemistry C* **2013**, *117*, 6702-6711.
11. Chen, X.; Chen, C.-B.; Udagama, Chammika N. B.; Ren, M.; Fong, Kah E.; Yung, Lin Y. L.; Giorgia, P.; Bettiol, Andrew A.; Watt, F., High-Resolution 3d Imaging and Quantification of Gold Nanoparticles in a Whole Cell Using Scanning Transmission Ion Microscopy. *Biophysical Journal* **2013**, *104*, 1419-1425.
12. Vasco, M. S.; Alves, L. C.; V., C.; Correia, D.; Godinho, C. P.; Sá-Correia, I.; Bettiol, A.; Watt, F.; Pinheiro, T., 3d Map Distribution of Metallic Nanoparticles in Whole Cells Using Mev Ion Microscopy. *Journal of Microscopy* **2017**, *267*, 227-236.
13. Rau, U.; Werner, J. H., Radiative Efficiency Limits of Solar Cells with Lateral Band-Gap Fluctuations. *Applied Physics Letters* **2004**, *84*, 3735-3737.
14. Ghorbani, T.; Zahedifar, M.; Moradi, M.; Ghanbari, E., Influence of Affinity, Band Gap and Ambient Temperature on the Efficiency of Cigs Solar Cells. *Optik* **2020**, *223*, 165541.
15. Abou-Ras, D., et al., Comprehensive Comparison of Various Techniques for the Analysis of Elemental Distributions in Thin Films. *Microscopy and Microanalysis* **2011**, *17*, 728-751.
16. Karydas, A. G.; Bogdanovic Radovic, I.; Streeck, C.; Kaufmann, C.; Caballero, R.; Rissom, T.; Kanngießner, B.; Beckhoff, B.; Jaksic, M.; Barradas, N. P., In-Depth Elemental Characterization of Cu(in,Ga)Se<sub>2</sub> Thin Film Solar Cells by Means of Rbs and Pixe Techniques. *Nuclear Instruments and Methods in Physics Research Section B: Beam Interactions with Materials and Atoms* **2014**, *331*, 93-95.

17. Kim, Y. I.; Kim, K. B.; Kim, M., Characterization of Lattice Parameters Gradient of Cu(In<sub>1-x</sub>Ga<sub>x</sub>)Se<sub>2</sub> Absorbing Layer in Thin-Film Solar Cell by Glancing Incidence X-Ray Diffraction Technique. *Journal of Materials Science & Technology* **2020**.
18. Iatosti, C.; Moret, M.; Tiberj, A.; Briot, O., Analysis of the Gallium Gradient in Cu(In<sub>1-x</sub>Ga<sub>x</sub>)Se<sub>2</sub> Absorbers by X-Ray Diffraction. *Solar Energy Materials and Solar Cells* **2021**, *220*, 110847.
19. Kong, Y.; Huang, L.; Chi, Z.; Wu, X.; Li, J.; Xiao, X., Failure and Recovery Modes of Submicron Cu(In,Ga)Se<sub>2</sub> Solar Cells with High Cu Content. *ACS Applied Materials & Interfaces* **2020**, *12*, 52857-52863.
20. Karydas, A. G.; Streeck, C.; Radovic, I. B.; Kaufmann, C.; Rissom, T.; Beckhoff, B.; Jaksic, M.; Barradas, N. P., Ion Beam Analysis of Cu(In,Ga)Se<sub>2</sub> Thin Film Solar Cells. *Applied Surface Science* **2015**, *356*, 631-638.
21. Jeynes, C.; Zoppi, G.; Forbes, I.; Bailey, M. J.; Peng, N. In *Characterisation of Thin Film Chalcogenide Pv Materials Using Mev Ion Beam Analysis*, 2009 International Conference on Sustainable Power Generation and Supply, 2009; 2009; pp 1-6.
22. Lindahl, J.; Zimmermann, U.; Szaniawski, P.; T, T.; Hultqvist, A.; Salomé, P.; Platzer-Björkman, C.; Edoff, M., Inline Cu(In,Ga)Se<sub>2</sub> Co-Evaporation for High-Efficiency Solar Cells and Modules. *IEEE Journal of Photovoltaics* **2013**, *3*, 1100-1105.
23. Jang, Y. J.; Lee, J.; Lee, K.-B.; Kim, D.; Lee, Y., Quantitative Analysis and Band Gap Determination for Cigs Absorber Layers Using Surface Techniques. *Journal of Analytical Methods in Chemistry* **2018**, *2018*, 6751964.
24. NREL Best Research-Cell Efficiency Chart, <https://www.nrel.gov/pv/cell-efficiency.html>. (accessed June, 2021).
25. Li, H.; Zhang, W., Perovskite Tandem Solar Cells: From Fundamentals to Commercial Deployment. *Chemical Reviews* **2020**, *120*, 9835-9950.
26. Alves, L. C.; Breese, M. B. H.; Alves, E.; Paúl, A.; da Silva, M. R.; da Silva, M. F.; Soares, J. C., Micron-Scale Analysis of Sic/Sicf Composites Using the New Lisbon Nuclear Microprobe. *Nuclear Instruments and Methods in Physics Research Section B: Beam Interactions with Materials and Atoms* **2000**, *161-163*, 334-338.
27. Grime, G. W.; Dawson, M., Recent Developments in Data Acquisition and Processing on the Oxford Scanning Proton Microprobe. *Nuclear Instruments and Methods in Physics Research Section B: Beam Interactions with Materials and Atoms* **1995**, *104*, 107-113.
28. Campbell, J. L.; Boyd, N. I.; Grassi, N.; Bonnicks, P.; Maxwell, J. A., The Guelph Pixe Software Package Iv. *Nuclear Instruments and Methods in Physics Research Section B: Beam Interactions with Materials and Atoms* **2010**, *268*, 3356-3363.
29. Jeynes, C.; Palitsin, V. V.; Grime, G. W.; Pascual-Izarra, C.; Taborda, A.; Reis, M. A.; Barradas, N. P., External Beam Total-Iba Using Data Furnace. *Nuclear Instruments and Methods in Physics Research Section B: Beam Interactions with Materials and Atoms* **2020**, *481*, 47-61.
30. Jeynes, C.; Barradas, N. P.; Szilágyi, E., Accurate Determination of Quantity of Material in Thin Films by Rutherford Backscattering Spectrometry. *Analytical Chemistry* **2012**, *84*, 6061-6069.
31. Salomé, P.; Fjällström, V.; Hultqvist, A.; Edoff, M., Na Doping of Cigs Solar Cells Using Low Sodium-Doped Mo Layer. *IEEE Journal of Photovoltaics* **2013**, *3*, 509-513.
32. Jeynes, C.; Barradas, N. P.; Rafla-Yuan, H.; Hichwa, B. P.; Close, R., Accurate Depth Profiling of Complex Optical Coatings. *Surface and Interface Analysis* **2000**, *30*, 237-242.
33. Butler, J. W., Criteria for Validity of Rutherford Scatter Analyses. *Nuclear Instruments and Methods in Physics Research Section B: Beam Interactions with Materials and Atoms* **1990**, *45*, 160-165.
34. Chu, W. K.; Meyer, J. W.; Nicolet, M. A., *Backscattering Spectrometry* Academic Press Inc.: London, 1978.

35. Jeynes, C.; Barradas, N. P.; Marriott, P. K.; Boudreault, G.; Jenkin, M.; Wendler, E.; Webb, R. P., Elemental Thin Film Depth Profiles by Ion Beam Analysis Using Simulated Annealing - a New Tool. *Journal of Physics D: Applied Physics* **2003**, *36*, R97-R126.
36. Metzger, W. K.; Repins, I. L.; Romero, M.; Dippo, P.; Contreras, M.; Noufi, R.; Levi, D., Recombination Kinetics and Stability in Polycrystalline Cu(in,Ga)Se<sub>2</sub> Solar Cells. *Thin Solid Films* **2009**, *517*, 2360-2364.
37. Abou-Ras, D.; Kostorz, G.; Romeo, A.; Rudmann, D.; Tiwari, A. N., Structural and Chemical Investigations of Cbd- and Pvd-Cds Buffer Layers and Interfaces in Cu(in,Ga)Se<sub>2</sub>-Based Thin Film Solar Cells. *Thin Solid Films* **2005**, *480-481*, 118-123.
38. He, X., et al., The Role of Oxygen Doping on Elemental Intermixing at the Pvd-Cds/Cu (Inga)Se<sub>2</sub> Heterojunction. *Progress in Photovoltaics: Research and Applications* **2019**, *27*, 255-263.
39. Mufti, N.; Amrillah, T.; Taufiq, A.; Sunaryono; Aripriharta; Diantoro, M.; Zulhadjri; Nur, H., Review of Cigs-Based Solar Cells Manufacturing by Structural Engineering. *Solar Energy* **2020**, *207*, 1146-1157.
40. Regesch, D.; Gütay, L.; Larsen, J. K.; Deprédurand, V.; Tanaka, D.; Aida, Y.; Siebentritt, S., Degradation and Passivation of Cuinse<sub>2</sub>. *Applied Physics Letters* **2012**, *101*, 112108.



TOC Graphic